https://doi.org/10.5194/egusphere-2026-4768
Preprint. Discussion started: 4 September 2026


# Crevasse distribution across Austrian Alpine glaciers linked to ice dynamics and surface topography

Celia A. Baumhoer[1], Selina Straßburger[1], Sarah Leibrock[1,2], Andreas J. Dietz[1] and Christoph Mayer[3]

[1]German Remote Sensing Data Center (DFD), Earth Observation Center (EOC), German Aerospace Center (DLR), Weßling, Germany
[2]Institute for Geography and Geology, University of Würzburg, D-97074 Wuerzburg, Germany
[3]Bavarian Academy of Sciences and Humanities, 80333 Munich, Germany

*Correspondence to*: Celia A. Baumhoer (celia.baumhoer@dlr.de)

**Abstract.** Glaciers flowing over uneven bed topography or undergoing extensional flow develop tensile stresses, and where these exceed the fracture strength of ice, crevasses open. Their distribution expresses the surface strain-rate field and enhances local ablation. Yet observations of where crevasses occur across Alpine glaciers remain scarce, and the theoretical controls on their formation, established largely from individual glaciers, are untested across a diverse glacier population. Here we present the first country-scale inventory of visible crevasses, mapped across all Austrian glaciers from high-resolution remote-sensing imagery, and analyse their spatial distribution and structural controls across six mountain regions. Crevasse density varies strongly between regions, peaking on the steep glaciers of the Zillertal Alps and the fast-flowing glaciers of the High Tauern, and reaching its lowest values on the large, low-gradient glaciers of the Ötztal and Stubai Alps. Linking crevasses to surface topography and ice dynamics, we show that crevassing is favoured by convex surfaces, steep slopes, and along-flow changes in slope. Ice-flow velocity and driving stress instead behave as thresholds, distinguishing highly crevassed terrain only once exceeded. We find no relationship with along-flow velocity change, despite longitudinal extension being the classical mechanism, indicating that much of the regional crevasse signal is inherited rather than locally generated and raising questions of advection and suppressed crevasse healing under reduced overburden pressure. The inventory supports route planning in published hiking maps and provides an observational basis for representing crevasse-enhanced heat exchange in mass-balance models and calibrating damage-mechanics schemes in ice-flow models.

## 1 Introduction

As glaciers flow over irregular bed topography or undergo extension where the flow accelerates, tensile stresses develop that can exceed the fracture strength of the ice, causing it to crack (Colgan et al., 2016). These fractures are called crevasses and their spatial distribution encodes valuable information about the stress regimes driving glacier deformation (van der Veen, 1998). Moreover, crevasses enhance local ablation by enlarging the melt-exposed surface area and altering the surface energy balance by enhancing turbulent heat fluxes (Colgan et al., 2016). Beyond their scientific value, crevasses also pose significant

https://doi.org/10.5194/egusphere-2026-4768
Preprint. Discussion started: 4 September 2026


hazards for mountaineers and field researchers working in glaciated terrain, making reliable crevasse detection and mapping a priority for both glaciology and operational safety (Baumhoer et al., 2025; Klocker et al., 2022).

A wide range of crevasse types exists, exhibiting diverse geometries and surface expressions. Crevasse dimensions in the Alps typically range from depths of several meters to 20–30 m, limited by viscous closure under lithostatic pressure (Ravanel et al., 2022). The maximum width of glacier crevasses based on field measurements ranges between 6–8 m. Crevasse length, however, can extend hundreds of meters (Ravanel et al., 2022). The spatial distribution of crevasse types within a glacier is governed by the interplay of topographic controls and ice-flow dynamics with systematic variations along the glacier's altitudinal gradient, reflecting differences between accumulation and ablation zones. Near the glacier head, bergschrunds develop where accelerating ice detaches from stationary firn, forming deep, headwall-parallel crevasses controlled by extensional separation. Down glacier in the accumulation zone, longitudinal extension drives the formation of transverse crevasses oriented perpendicular to flow. On steep gradients, these develop into icefalls. In confined valleys, lateral drag induces shear zones that generate marginal splaying crevasses at a ~45° angle to the flow direction. Toward the terminus, ice deceleration and lateral spreading produce longitudinal crevasses parallel to flow, transitioning to radial splaying crevasses where unconfined expansion dominates. Crisscrossed fracture networks ("tic-tac-toe" patterns) indicate flow in two directions caused by bedrock irregularities. Circular crevasses have been observed with increasing frequency in the Alps in recent years, with documented occurrences linked to collapse features resulting from subglacial cavity failure and the subsidence of meltwater channels (Hösli et al., 2025). A visual representation of different crevasse types is illustrated in Figure 1.

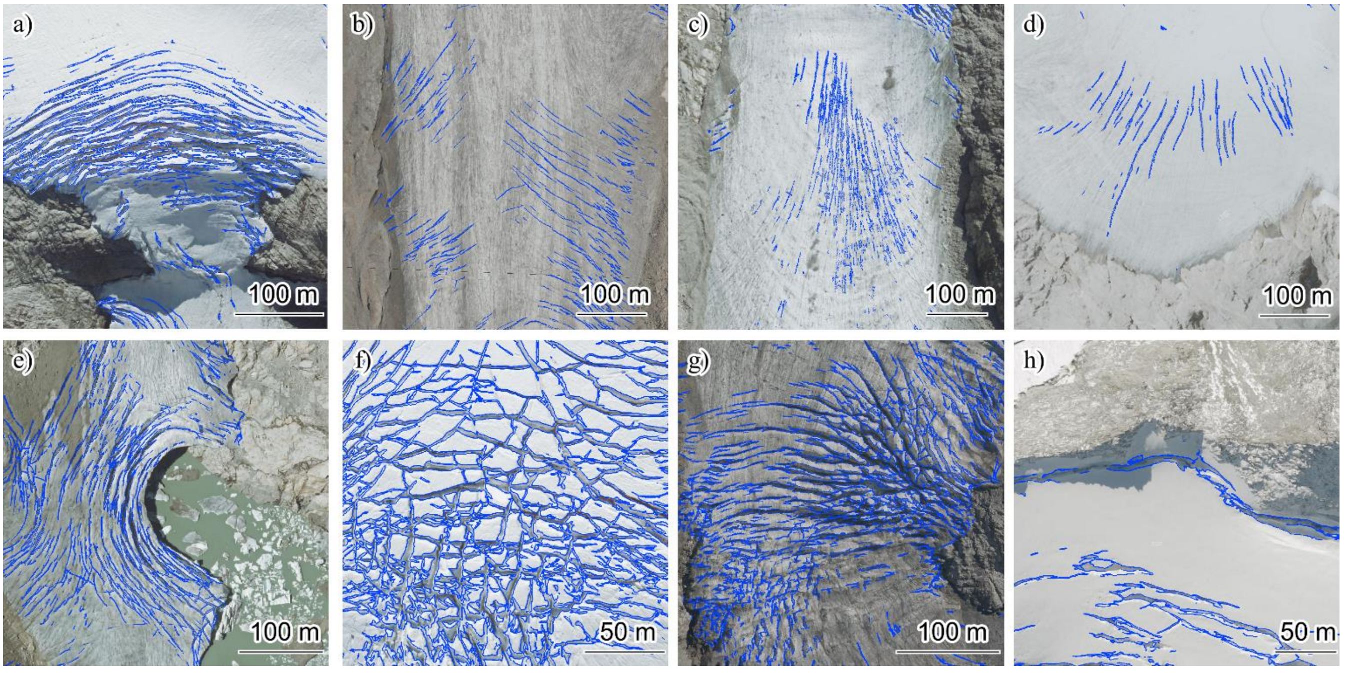


**Figure 1: Different crevasse types in the Austrian Alps mapped on aerial imagery. (a) Transverse crevasses at Obersulzbachkees, (b) marginal splaying crevasses at Gepatschferner, (c) longitudinal crevasses at Obersulzbachkees**

https://doi.org/10.5194/egusphere-2026-4768
Preprint. Discussion started: 4 September 2026


**transitioning to splaying crevasses, (d) radial splaying crevasses at the glacier margin at Hallstätter Gletscher, (e) Circular Crevasses at Unterer Keesboden, (f) "tic-tac-toe" crevasse patterns at Krimmlertörlkees, (g) ice fall at Gepatschferner, and (h) Bergschrund at Waxeggkees. Glacier flow is directed towards the bottom of the image.**

The distribution of crevasses along the glacier's altitudinal gradient reflects how the ice is stressed as it flows. Glacier ice responds to stretching in two ways: at low rates it deforms slowly and continuously, but when it is stretched faster than it can deform, the brittle surface ice fractures and a crevasse opens. Crevasses therefore mark the places where the tensile strain rate exceeds the critical value at which the ice fails rather than flows. This rate is set not by the absolute flow speed but by how that speed changes from one place to the next as the strain rate is the spatial gradient of velocity, so ice that moves rapidly yet uniformly experiences little deformation and can remain largely intact despite its high speed. Crevasse density thus traces the strain-rate field rather than the velocity field itself (Colgan et al., 2016; Harper et al., 1998; Vaughan, 1993). The strain-rate field is governed largely by the underlying bed and surface topography. Where the surface steepens or becomes convex, the ice accelerates and is stretched in the flow direction, generating the extensional stresses that open dense fields of transverse crevasses. Steep surface gradients also raise the driving stress, further favouring fracture. Where the surface flattens or becomes concave, by contrast, the flow is compressional, viscous creep dominates over fracture, and existing crevasses tend to close and heal (Colgan et al., 2016).

Despite their glaciological significance, comprehensive observational datasets describing crevasse distribution on mountain glaciers remain limited, largely due to the logistical complexity and labour-intensive nature of field-based surveys. Remote sensing provides a valuable data source to map crevasses over large spatial extents (Baumhoer et al., 2025; Surawy-Stepney et al., 2023) as Figure 2 illustrates. However, large-scale applications have been constrained by the limited availability of high-resolution imagery capable of resolving narrow Alpine crevasses and by the substantial time and effort required for manual delineation from optical data.

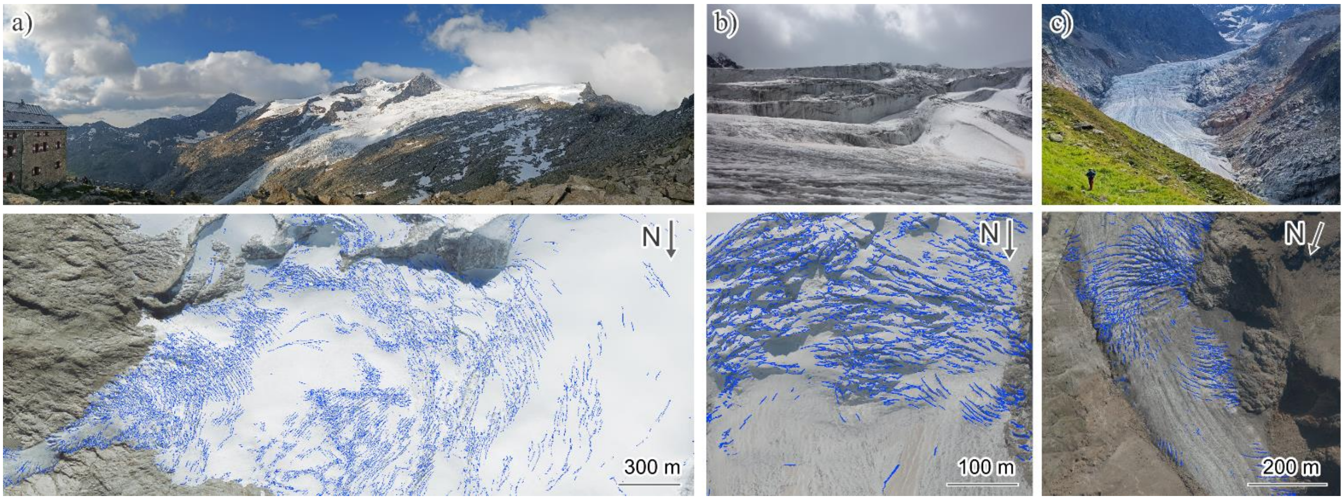


**Figure 2 Examples of glacier crevasses in the field and mapped from orthophotos. (a) Schlatenkees below Großvenediger (aerial: 2022, photo: 2025), (b) Taschachferner below Wildspitze (aerial: 2020, photo: 2021), and (c) Gepatschferner below Weißseespitze (aerial: 2020, photo: 2021). Photos: C. Baumhoer. Aerial imagery: basemap.at.**

Automating the detection of surface crevasses from remote sensing imagery can significantly reduce effort, but it remains highly challenging due to similarities with other surface features, the need for high-resolution data, and variable illumination conditions (Colgan et al., 2016; Izeboud and Lhermitte, 2023; Shankar et al., 2023). The first automated approaches have been developed for ice shelves and outlet glaciers, as the resolution of freely available satellite data such as Sentinel-1, Sentinel-2 or Landsat is sufficient due to the presence of large crevasses (Izeboud and Lhermitte, 2023; Surawy-Stepney et al., 2023; Van Wyk de Vries et al., 2023). Conventional crevasse detection methods use changes in the backscatter signal to identify crevasses in TerraSAR-X imagery (Marsh et al., 2021), brightness changes identified by different filters in ASTER imagery (Xu et al., 2011), Gabor filters for Sentinel-2 data (Van Wyk de Vries et al., 2023), processing-intensive Sentinel-1 interferograms and a Canny edge detection algorithm (Libert et al., 2022) or by calculating residuals between a high-resolution DEM and its smoothed version (Chudley et al., 2021). More recent approaches exploit the advantage of deep learning and detected crevasses on Antarctic ice shelves with U-Net like architectures (Lai et al., 2020; Surawy-Stepney et al., 2023; Zhao et al., 2022). First approaches have been made to use AI-driven foundation models trained for general image processing tasks for crevasse detection. Kirillov et al. (2023) mapped different glacial features with the Segment Anything Model (SAM) but could not produce accurate results (F1-score 44 %) for crevasses even when using manual prompts. Despite initial progress in crevasse detection on ice sheets, there are hardly any studies on the detection of crevasses in mountain glaciers. Ground penetrating radar (GPR) has been used to detect crevasses in mountainous areas (Eder et al., 2008; Zamora et al., 2007). While GPR is a valuable tool for this purpose, it requires fieldwork and is best suited for smaller, localized studies. One example is a study conducted on the Shaune Garang Glacier in the Himalayas, which employed pan-sharpened thermal and short-wave infrared Landsat imagery at 15 m spatial resolution and validated results against GPS field measurements, achieving a root-mean-square error of 6.32 m for crevasse length estimates (Bhardwaj et al., 2016). A more recent study focused on Alpine glaciers

https://doi.org/10.5194/egusphere-2026-4768
Preprint. Discussion started: 4 September 2026


in the Stubai and Ötztal Alps, where crevasse mapping was performed across all glaciers using high-resolution orthophotos. This work applied a multitask deep learning architecture (HED-UNet) for automated detection, achieving an overall accuracy of 86.2%, and demonstrating significantly improved scalability and feature extraction capability compared to earlier approaches (Baumhoer et al., 2025).

An alternative to observation-based mapping of crevasse distribution is provided by physically based fracture mechanics models. These models are theoretical frameworks for predicting crevasse formation through stress analysis and fracture toughness criteria (van der Veen, 1998; Colgan et al., 2016; Grinsted et al., 2024) or geometric information (Dobler et al., 2023). However, these continuum-mechanical approaches demand precise input data e.g. on ice thickness, which is difficult to derive on large-scale (Dobler et al., 2023). Consequently, the combination of labor-intensive manual mapping from satellite imagery and the complexity of glacier models has hindered the development of spatially consistent crevasse inventories. As a result, comprehensive datasets of crevasse distribution remain scarce. This limits quantitative analyses of crevasse distribution and hinders robust assessment of the factors controlling their formation and spatial patterns. To address this gap, we present the first glacier-wide crevasse inventory for the Austrian Alps, using automated detection methods to systematically characterize crevasse distribution and link it to surface geometry and ice flow velocity. Building on the deep learning framework of Baumhoer et al. (2025), we extend automated crevasse mapping to all Austrian glaciers, generating a country-scale dataset that enables statistical analysis of fracture patterns across diverse glaciological morphologies.

This study pursues two objectives: (1) to characterise the spatial distribution of crevasses across Austrian mountain glaciers and identify dominant regional patterns, and (2) to assess the degree to which observable variables such as surface topography and ice dynamics explain crevasse occurrence. We hypothesise that crevasse density scales with slope steepness, surface convexity, and ice flow velocity, in line with theoretical expectations for stress-driven fracture in flowing ice. To address these objectives, we present the first systematic, country-wide crevasse inventory for Austrian glaciers, derived from high-resolution aerial orthophotos using computer vision techniques. Topographic attributes from a digital elevation model and surface velocity fields are then integrated to quantify differences in controlling factors between minimally and highly crevassed glacier zones. The resulting inventory provides empirical constraints for stress-based fracture models, informs crevasse-enhanced ablation parameterisations in mass balance studies, and offers practically relevant information for glacier traverse planning and field safety.

## 2 Materials and Methods

### 2.1 Data preparation

We detect crevasses based on aerial orthophotos acquired between 2019 and 2022 over Austria with a spatial resolution of 20 cm. The entire glaciated area is covered by orthophotos acquired over a four-year time period due to the regular repeat-cycle of orthophoto acquisitions over Austria. Imagery is usually acquired in the end of summer with the lowest possible snow cover in the mountains. This time at the end of the ablation season is best suited to identify crevasse areas. Still, in the higher elevation

https://doi.org/10.5194/egusphere-2026-4768
Preprint. Discussion started: 4 September 2026


areas with permanent snow cover crevasses may be hidden under snow bridges which cannot be detected from optical remote sensing imagery. For each federal state we acquired all available RGB orthophotos over glaciated area from their open access GIS services (see data availability section). For Salzburger Land, no open access orthophotos are available therefore imagery was downloaded from the WMTS orthophoto service called basemap.at. Overall, 1,567 orthophoto scenes and additional scenes for Salzburger Land were downloaded to cover Austria's glaciers. As reference for glacier boundaries we used the dataset by the Bundesamt für Eich- und Vermessungswesen (BEV) which was updated for the year 2023 and covers a glaciated area of 329.55 $km^2$ (BEV, 2024). The BEV boundaries were used to mask each orthophoto scene for glaciated areas to focus solely on glaciers. The extent of glaciated area across Austria is shown in Figure 3 in light blue.

## 2.2 Glacier crevasse detection

We detect glacier crevasses from high-resolution orthophotos by using the method described in Baumhoer et al. (2025). Here, we give a short summary of the method applied. We use the multitask Convolutional Neural Network (CNN) HED-Unet (Heidler et al., 2021) to detect the boundaries of glacier crevasses from high-resolution imagery. The advantage of a multitask model is the ability to extract features by image segmentation and boundaries by edge detection. Both tasks are performed simultaneously to update the model weights jointly based on the segmentation and edge detection task. The encoder-decoder model architecture consists of six up- and downsampling blocks. The encoder extracts feature maps at varying resolutions through downsampling, capturing contextual information, which is subsequently reintroduced to the original image resolution by the decoder through upsampling and skip connections. However, due to the creation of deep feature pyramids, the model may overlook feature maps at the lowest resolution. To address this, deep supervision is applied, generating multiscale ground truth predictions that enhance the model's receptive field and promote better capture of structures across all pyramid resolutions. The final classification results for edge detection and segmentation tasks are obtained by combining predictions from different pyramid levels using hierarchical attention merging, which selectively focuses on different resolutions within the pyramid. This mechanism enables the model to incorporate both large-scale information for locating crevasse zones on a glacier and small-scale details for accurate crevasse boundary detection. The original HED-Unet model by Heidler et al. (Heidler et al., 2021) was adapted to take three channel RGB imagery as input instead of SAR data, applied a global normalization and percentile clip to enhance image properties and decreased the tile size from 768 x 768 to 512 x 512 pixels to allow training with larger batch sizes. For model inference (prediction of glacier crevasses with a previously trained model), we use the model weights trained in the study by Baumhoer et al. (2025). The training data is based on 16 different hand-labelled orthophotos in the Stubai and Ötzal Alps as well as over Großvenediger covering glacier crevasse morphologies typical in Austria. For this study, we used the best trained model defined by the lowest validation loss (0.048) at epoch 86, which achieved an edge accuracy of 98.7% on both training and validation data. Inference was performed on 2048 x 2048 pixel tiles with an overlap of 265 pixels to maximize GPU efficiency and reducing the prediction time to one minute per scene.

https://doi.org/10.5194/egusphere-2026-4768
Preprint. Discussion started: 4 September 2026


### 2.3 Validation

The detection approach follows Baumhoer et al. (2025) in which the method was validated against manually mapped crevasses and achieved a balanced accuracy of 86.2%, a weighted F1 score of 98.4% and a macro-averaged F1 score of 78.5% under comparable alpine conditions. The macro-averaged recall with 86.3% is higher than the precision of 73.7% indicating that the detection of crevasses is robust and it is less likely that crevasses are overlooked. Thus, the lower precision indicates an overprediction of crevasses in some cases. Visual inspection reveals that most false predictions occur in edge regions of the glaciers where the glacier boundaries to mask the orthophotos were not sufficiently up to date and structures in the rock were detected instead. While no independent quantitative validation was conducted at the country-wide scale of the present inventory, the consistency of input data quality across the study domain and the homogeneous acquisition parameters of the orthophoto dataset support the transferability of reported accuracy estimates to the broader application presented here. To further substantiate result reliability at scale, a systematic manual visual check of the full inventory was performed, confirming overall detection plausibility and identifying only systematic misclassification patterns across outdated glacier boundaries due to rapid glacier retreat. We address this issue by manually flagging areas (on a hexagonal basis) completely covered by debris or rock due to glacier retreat and exclude these regions from our analysis.

### 2.4 Post-processing of the crevasse dataset

The inference outputs are raster files with prediction probabilities for crevasse boundaries. The boundaries have different widths and several intersections comparable to hand drawn crevasses. To ensure every crevasse boundary is weighted equally, the prediction probabilities are binarized at a threshold of 0.5. All prediction patches are merged into region-wide rasters, and in overlapping areas the average is taken. The Austrian mountain regions are defined by the GMBA Mountain Inventory version 2 Level 8 (Snethlage et al., 2022). Level 8 includes the regions Dachstein, Hohe Tauern, Oetztaler Alpen, Silvretta, Stubai and Zillertaler Alpen over Austria. The spatial extent of the different GMBA regions is shown in Figure 3. After merging, crevasse boundaries are thinned so each boundary has a unified width of one pixel (20 cm) allowing for consistent density calculations.

### 2.5 Crevasse density, surface geometry and ice flow velocity

This is an observation-based study that relates three independent observational datasets: a digital elevation, from which surface slope and curvature are derived, a satellite-derived surface ice-flow velocity product, and the crevasse inventory produced within this study. All analyses are performed on these observations rather than on numerical modelling of ice dynamics or fracture. To analyse surface geometric and ice flow velocity controls on crevasse distribution, we aggregated spatial data using Uber's H3 hexagonal geospatial indexing system (h3-py library for Python). We selected resolution 11 hexagons (approximately 2,125 m² each) to match the coarsest input dataset (ice flow velocity at 50 m spatial resolution). Within each hexagon, topographic and ice-dynamic variables were averaged by their median values within each hexagon to minimize

https://doi.org/10.5194/egusphere-2026-4768
Preprint. Discussion started: 4 September 2026


sensitivity to outliers. Topographic controls were derived from Austria's 2022 Digital Terrain Model (DTM), acquired via airborne laser scanning at 1 m native resolution. Slope (in degrees) and profile curvature were calculated using the Python package RichDEM (Barnes, 2016) following the method of Zevenbergen and Throne (1987). Profile curvature and slope were calculated for a spatial resolution of 50 m to match the resolution of the velocity data and smooth out topographical variations created by crevasses themselves. Ice-dynamic control is quantified using surface velocities derived from Sentinel-2 feature tracking for the 2020–2021 hydrological year (Rabatel et al., 2023), selected to temporally align with the imagery used for crevasse mapping. Velocity data an ice flow direction, available at 50 m resolution, contain spatial gaps; notably, no observations exist for the Dachstein Mountains, which are therefore excluded from the flow velocity analysis.

Driving stress ($\tau_{di}$) is calculated similar to Dobler et al. (2023) where driving stress is a function of the glacier density ρ, the gravity *g*, the ice thickness *h* and the glacier surface slope α:

$$\tau_{di} = \rho \times g \times h \times \sin\alpha$$

Geographic gradients (velocity, slope, stress) were computed with numpy.gradient (second-order central differences, one-sided at grid edges), negating the row derivative to account for the southward-increasing row index. The along-flow derivative of a field was obtained by projecting this gradient onto the unit surface-velocity vector, giving a signed quantity that is positive where the field increases down glacier.

Crevasse density was computed as the total count of crevasse boundary pixels within each hexagon, yielding a theoretical maximum of 53,125 pixels per hexagon. We classified hexagons based on the crevasse density and the attributes ‘rock’ and ‘snow’ into different categories. First, hexagons clearly outside of the current glacier extent or with heavy debris cover were manually assigned the attribute ‘rock’ and excluded from the analysis as debris covered and rock areas are prone to misclassifications (see 2.3 Validation). Second, all areas that were snow covered during the image acquisition were tagged and areas with no crevasses detected but snow covered were assigned to the class ‘snow’ as potential crevasses below snow bridges may exist. To enable comparative analysis, glacier areas were classified into three crevasse density categories based on percentile thresholds. Areas below the 10th percentile (below 50 boundary pixels) were classified as crevasse-free, areas between the 10th and 75th percentile as crevassed, and areas above the 75th percentile (above 1220 boundary pixels) as highly crevassed. The lower threshold was chosen to exclude areas with negligible detected fracturing, thereby reducing the influence of detection artifacts on the analysis. The upper threshold identifies zones of intense fracturing where crevasse density is sufficiently elevated to allow meaningful comparison of topographic and dynamic controls.

Differences in topographic and ice-dynamical parameters between crevasse density classes were quantified using Cliff's delta, a non-parametric effect size based on the ordering of observations. Cliff's delta was preferred over standardised mean-difference measures such as Cohen's d because the parameter distributions are non-normal and the classes differ markedly in size and variance, conditions under which standardised mean differences are biased (Meissel and Yao, 2024). Delta ranges from −1 to +1, where 0 indicates complete distributional overlap and ±1 complete separation, with the sign indicating the direction of the difference. Magnitudes were interpreted as negligible ($|\delta| < 0.11$), small ($\geq 0.11$), medium ($\geq 0.28$) and large ($\geq 0.43$). Each crevasse density class was compared against the crevasse-free class as reference.

https://doi.org/10.5194/egusphere-2026-4768
Preprint. Discussion started: 4 September 2026


# 3 Results

## 3.1 A glacier crevasse dataset of the Austrian Alps

This study provides the first glacier crevasse dataset for the Austrian Alps. The dataset covers Austria's entire glaciated area and is split into the six main Austrian mountain regions. Figure 3 provides examples of the Austrian-wide dataset with crevasses detected over the different mountain regions. Over Taschachferner transverse crevasses are clearly visible in the middle part of the glacier whereas marginal crevasses are present further downstream towards the glacier tongue (Figure 3a). Heavily crevassed areas are visible over the Untersulzbachkees at the Großvenediger. Transverse crevasses are clearly visible even though most of the glacier is snow covered (Figure 3b). The glaciers in the Dachstein mountains are very small and crevasses appear mostly at the lower half of the glacier. Transvers and longitudinal crevasses are present in the middle part of the glacier whereas splaying crevasses are present close to the glacier tongue (Figure 3c). Crevasse patterns for the Jamtalferner are more diffuse. In the upper part of the glacier transverse crevasses dominate whereas in the lower part at the borders and tongue diffuse patterns of longitudinal, crossed and splaying crevasses are present. Especially at the tongue transverse, splaying and longitudinal crevasses interfere and might be remnants due to glacier retreat (Figure 3d). Similar to the Taschachferner, the Gepatschferner has clear transverse crevasses in the upper part and splaying crevasses at the glacier tongue (Figure 3e). Pasterzenboden is snow covered and heavily crevassed where transverse crevasses transition into crossed and longitudinal crevasses. Glacier retreat is clearly visible leaving large crevasses close to the rock (Figure 3f). The glaciers below Hoher Sonnblick are small and snow covered. Clear transverse crevasses are visible as well as cracks in all direction in the ice which formed due to the floating glacier tongue in the glacial lake at Glodbergkees (Figure 3g).

https://doi.org/10.5194/egusphere-2026-4768
Preprint. Discussion started: 4 September 2026


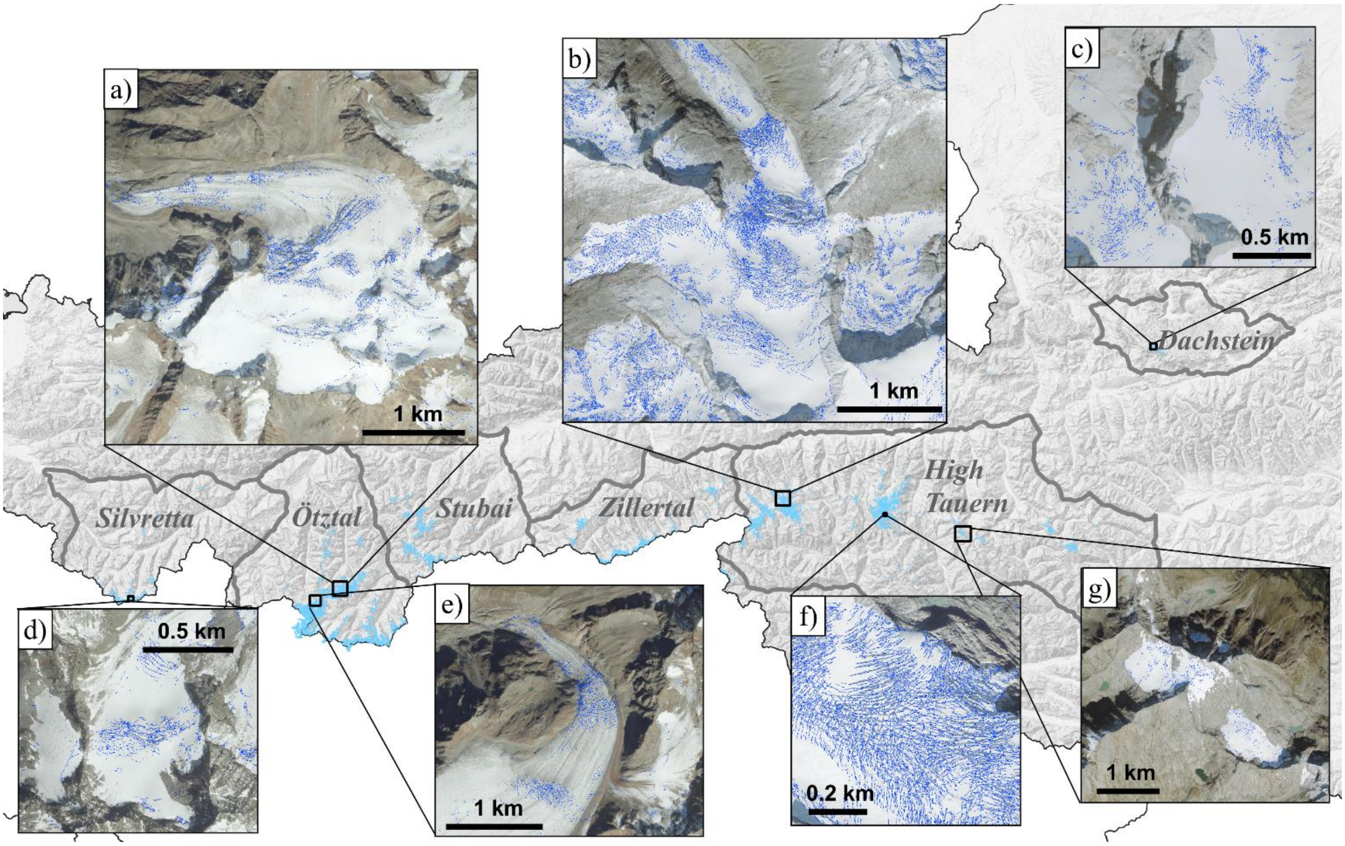


**Figure 3 Examples of glacier crevasses detected on Austrian glaciers (light blue) with insets for (a) Taschachferner at Wildspitze, (b) Untersulzbachkees at Großvenediger, (c) Großer Gosaugletscher and Hallstätter Gletscher at Hoher Dachstein, (d) Jamtalferner at Dreiländerspitze, (e) Gepatschferner at Weißseespitze, (f) Pasterzenboden at Großglockner, and (g) Glodbergkees and Kleinfleißkees at Hoher Sonnblick. Aerial imagery: basemap.at.**

## 3.2 Spatial distribution of glacier crevasse density in the Austrian Alps

Regional crevasse distribution (summarized in Table 1 and visualized in Figure 4) reveals strong contrasts in both absolute area and fractional coverage across the six mountain regions (all bracketed values represent interquartile ranges). The highest absolute crevasse density (10,501 boundary pixels per hexagon) was recorded on the Karlinger Kees in the High Tauern, where icefalls locally generate extreme density values. At the regional scale, the Zillertal Alps exhibit the highest median crevasse density (854.5 [319.0–1,832.5]), marginally exceeding the High Tauern (720.0 [247.0–1,631.5]). In contrast, the lowest median densities occur in the Ötztal Alps (178.0 [70.0–444.0]), followed by the Stubai Alps (239.0 [88.0–637.0]) and the Silvretta Alps (239.5 [86.8–564.8]).

In terms of fractional coverage, the Zillertal Alps and High Tauern show the highest proportions of crevassed area (58.2% and 56.6%, respectively) and highly crevassed area (23.4% and 20.6%, respectively). However, in absolute terms the High Tauern dominate markedly, with 63.6 km² of crevassed area compared to only 15.3 km² in the Zillertal Alps, reflecting the substantially larger total glacier area of the former. At the opposite end, the Ötztal and Stubai Alps exhibit the lowest crevassed fractions

https://doi.org/10.5194/egusphere-2026-4768
Preprint. Discussion started: 4 September 2026


(20.9% and 24.4%) and negligible highly crevassed extents (2.0% and 3.5%). Snow cover during the mapping period was broadly similar across most regions (20.6–29.0%), with the notable exception of the Dachstein mountains, where 58.0% of glacier area was snow-covered. This elevated snow fraction likely caused underestimation of crevasse extent there due to bridging, and results from this region should be interpreted with corresponding caution.

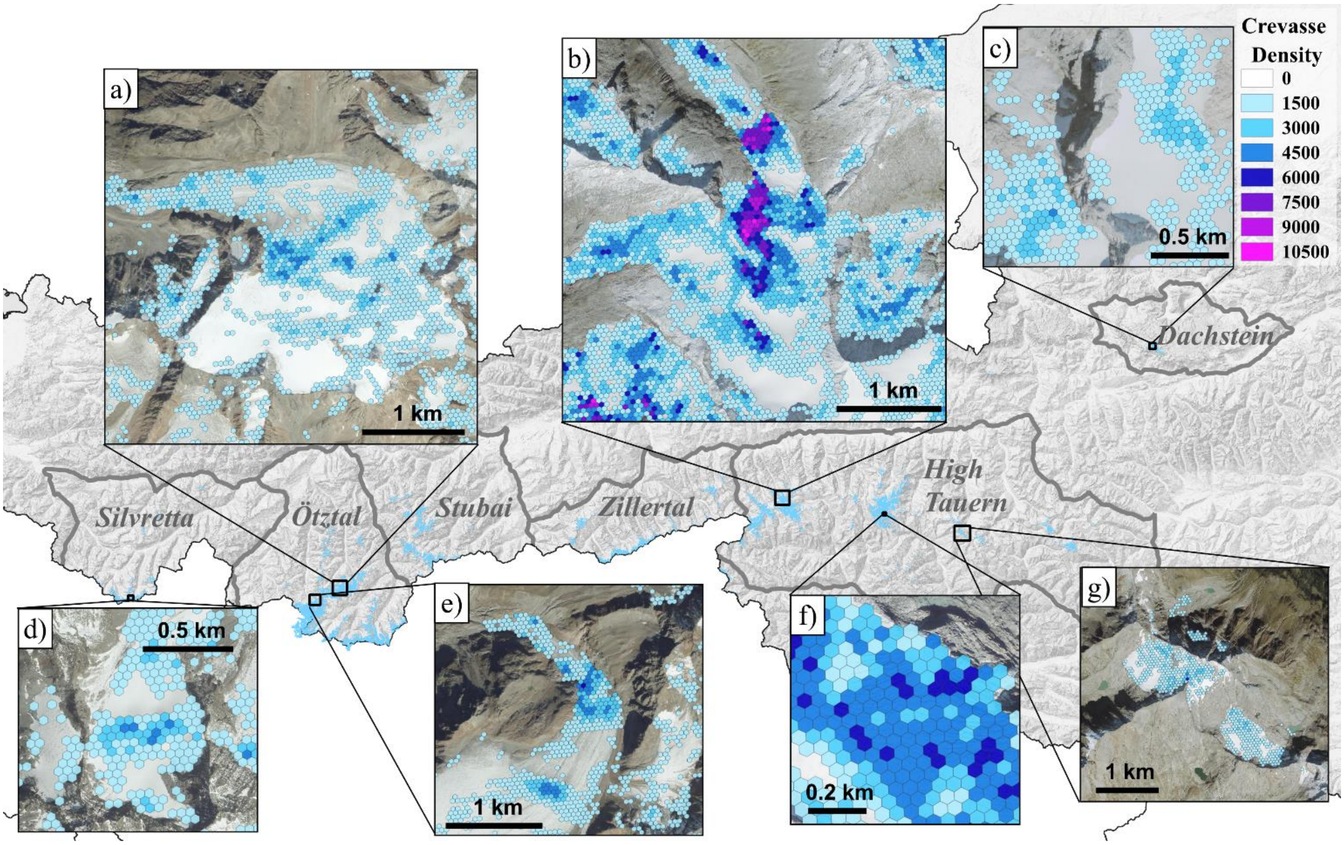


**Figure 4 Crevasse densities calculated for Austrian glaciers. Densities are given as number of crevasse boundary pixels within one hexagon. Insets match Figure 3. Aerial imagery: basemap.at.**

https://doi.org/10.5194/egusphere-2026-4768
Preprint. Discussion started: 4 September 2026


**Table 1 Crevasse density statistics for Austrian mountain regions. Values reported include the median crevasse density with interquartile range (IQR), maximum density, and the proportion of glaciated area affected by crevassing. Also shown are the absolute areas classified as crevasse-free and crevassed, as well as the percentage of crevassed area that is classified as highly crevassed. Crevassed area is calculated based on the number of hexagons with a crevasse density higher than 50 ($10^{th}$ Quantile). Maximum values in bold, minimum values underlined.**

| Region | median (IQR) | max density | crevasse free [km²] | snow [km²] | crevassed [km²] | highly crevassed [km²] | snow [%] | crevassed [%] | highly crevassed [%] |
|---|---|---|---|---|---|---|---|---|---|
| **Dachstein** | 258.5 (95.8–681.8) | 3402 | 0.4 | 2.5 | 1.5 | 0.2 | **58.0** | 33.3 | 5.0 |
| **High Tauern** | 720.0 (247.0–1631.5) | **10501** | 16.3 | **32.6** | **63.6** | **23.2** | 29.0 | 56.6 | 20.6 |
| **Silvretta** | 239.5 (86.8–564.8) | 4364 | 4.2 | 2.8 | 4.2 | 0.5 | 24.7 | 37.6 | 4.4 |
| **Stubai** | 239.0 (88.0–637.0) | 5381 | 17.6 | 6.6 | 7.8 | 1.1 | 20.6 | 24.4 | 3.5 |
| **Zillertal** | **854.5 (319.0–1832.5)** | 5994 | 4.0 | 6.9 | 15.3 | 6.1 | 26.4 | **58.2** | **23.4** |
| **Ötztal** | 178.0 (70.0–444.0) | 4866 | **68.2** | 30.0 | 26.0 | 2.5 | 24.2 | 20.9 | 2.0 |
| **Austria** | 444.0 (136.0–1220.0) | 10501 | 110.7 | 81.4 | 118.3 | 33.7 | 26.2 | 38.1 | 10.8 |

### 3.3 Linking crevasse distribution to surface topography and ice dynamical controls

Figure 5 presents forest plots of Cliff's delta effect sizes for topographic and dynamic controls on crevasse formation. Median values for each variable were compared against crevasse-free areas to quantify differences using Cliff's delta.

Notable differences in elevation were observed among classes (Figure 5a). Snow-covered areas exhibited a median elevation 127 m higher than crevasse-free areas, corresponding to a medium effect size (Cliff's delta $\delta = 0.38$). Conversely, highly crevassed areas showed a median elevation 78 m lower than crevasse-free areas, reflecting a small effect size ($\delta = 0.20$). The difference in median elevation between crevassed and crevasse-free areas was negligible (−5.0 m).

Highly crevassed areas were located on more convex surfaces, showing a medium effect size ($\delta = 0.36$), followed by crevassed areas with a small effect size ($\delta = 0.24$). Snow-covered areas were predominantly located on flat surfaces. For concave surface topography, differences among all crevasse classes were negligible, with the lowest Cliff's delta observed for highly crevassed areas ($\delta = 0.13$).

Absolute slope exhibited the highest effect size found in this study, for crevasse-free versus highly crevassed areas ($\delta = 0.42$). Crevasse density increased with slope steepness where crevassed areas were located on slopes that were, in median, 5.5° steeper than crevasse-free areas, while highly crevassed areas were located on slopes, in median, 8.1° steeper than crevasse-free areas. Slope change along flow (either steepening or flattening) also exerted control on crevasse distribution, with a small effect size between crevasse-free and highly crevassed areas ($\delta = 0.22$). All other differences were negligible.

Absolute velocity was a control for highly crevassed areas, with a small effect size ($\delta = 0.21$). A similarly small effect size was found between snow-covered areas in the accumulation zone and crevasse-free areas ($\delta = 0.19$). In contrast, along-flow velocity change had no discernible effect on the degree of crevassing overall. Only snow-covered areas were located in zones of the strongest velocity change, with small effect sizes for both compressive ($\delta = 0.19$) and extensional ($\delta = 0.17$) flow

https://doi.org/10.5194/egusphere-2026-4768
Preprint. Discussion started: 4 September 2026


regimes. Driving stress showed a small effect size for highly crevassed versus crevasse-free areas, for both uphill (δ = 0.18) and downhill (δ = 0.22) orientations and all other differences were negligible. The driving stress gradient indicating areas of changes in driving stress proved a slightly stronger control factor, with a Cliff's delta of 0.24 between highly crevassed and crevasse-free areas.

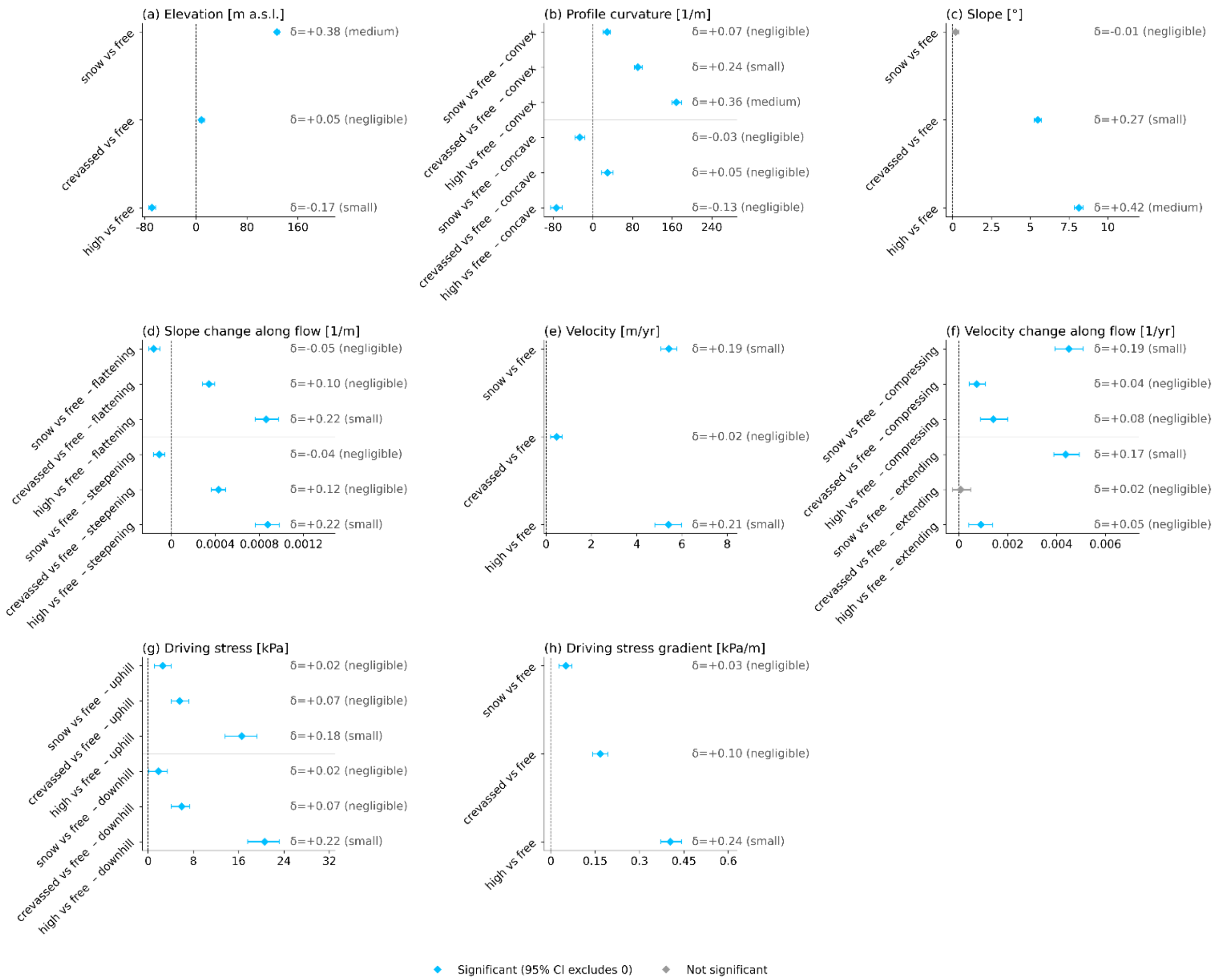


**Figure 5 Cliff's delta effect sizes for topographic and dynamic controls on crevasse formation. (a) Elevation, (b) profile curvature, (c) slope, (d) slope along flow, (e) velocity, (f) velocity change along flow, (g) driving stress, and (h) driving stress gradient.**

## 4 Discussion

### 4.1 A first country-scale crevasse inventory for mountain glaciers

The glacier crevasse dataset presented here is the first systematic, spatially consistent crevasse inventory at country scale for mountain glaciers, moving beyond individual glacier case studies and regional subsets (Bhardwaj et al., 2016; Dobler et al., 2023). It is openly available and provides, for the first time, crevasse information with a documented source and acquisition date in contrast to existing cartographic mappings, for which the underlying metadata (satellite imagery, aerial photography, or field survey) and timing are often unknown. As the first vector representation of Austrian glacier crevasses, it enables quantitative spatial analysis that printed maps cannot support. The fully automated mapping framework is readily reproducible and transferable to other heavily glacierised regions with available aerial imagery such as Switzerland and France. Beyond its descriptive value, the inventory maps zones of extensional flow and elevated latent heat exchange that can serve as an observational constraint for ice-flow and surface mass-balance models.

The dataset coverage provides a sample size large enough to separate the relative importance of elevation, slope, curvature, and ice flow velocity through frequency-distribution analysis, across a topographically diverse range of glaciers mapped with a single, consistent methodology. This reveals systematic regional contrasts for the first time in crevasse distribution. For instance, the high densities and extensive crevassed areas of the High Tauern and Zillertal Alps versus the markedly lower values of the Ötztal and Stubai Alps.

### 4.2 Topographic and dynamic controls on crevasse distribution

The mechanics of crevasse formation are well established at the scale of individual glaciers. Crevasses open where tensile stress exceeds the fracture strength of ice, concentrating in zones of extensional flow over steep or convex topography (Nye, 1952; Harper et al., 1998; Colgan et al., 2016). These controls, however, derive almost exclusively from intensive studies of single glaciers or small glacier complexes (Harper et al., 1998; Dobler et al., 2023), where dense stake networks or high-resolution photogrammetry resolve the deformation field at a few tens of metres. Whether they survive the transition to a topographically and climatically diverse glacier population, observed with the coarser data available at regional scale, has not been tested. Our country-scale inventory, combined with surface topography and ice-dynamical parameters, provides such a test.

Crevasse density increases with surface convexity (Fig. 5b). This was already postulated by Nye (1952) and was recovered at the glacier scale by Dobler et al. (2023), who found crevassed areas on Vernagtferner preferentially in convex terrain.

Convexity alone, however, is not diagnostic. Thresholding on curvature leaves a substantial fraction of mapped crevassed area undetected, reproducing the behaviour Dobler et al. (2023) reported at Vernagtferner, where the optimal curvature threshold recovered 48 % of crevassed area while misclassifying 14 % of the glacier surface. Our results extend that finding where 64.5% of high crevasse density hexagons were located on convex surface and 47.2% of the crevassed polygons whereas 34.6% crevasse free polygons were located on convex surfaces (see Figure A 2 in the appendix).

https://doi.org/10.5194/egusphere-2026-4768
Preprint. Discussion started: 4 September 2026


With still about one third of highly crevassed areas found on concave slopes there are two plausible explanations. The first is the bergschrund and its associated fractures, which form on the concave slopes typical of accumulation-area headwalls. The second is subglacial cavity collapse. Hösli et al. (2025), in a Swiss-wide inventory, describe collapse depressions ringed by circular crevasses, formed where a growing subglacial cavity causes the ice roof to fail, with downwasting and shallow ice as prerequisites. Both produce crevasses that are gravity-driven rather than flow-driven, and both are invisible to a stress-based predictor.

Surface slope is the strongest single discriminator, with Cliff's delta medium for highly crevassed areas ($\delta = 0.42$) and small for crevassed ($\delta = 0.27$) areas. Slope changes along flow have a small effect size for highly crevassed areas ($\delta = 0.22$) but is negligible for slightly crevassed areas. This indicates higher crevasse densities in areas where the slope is flattening or steepening. But only the latter is expected from extensional flow whereas the former suggests crevasses formed up-glacier that have not yet closed on entering the flatter reach, and is our first indication that part of the regional signal is inherited rather than local which we elaborate below.

Highly crevassed areas occur at a median velocity of 18.0 m $a^{-1}$, whereas crevasse-free and slightly crevassed areas share near-identical medians of 12.6 and 13.0 m $a^{-1}$. Velocity therefore discriminates the intensity of crevassing but not its presence potentially indicating zones of crevasse formation. Additionally, to median flow speed, we computed the along-flow velocity change as a proxy for longitudinal extension because crevasses would be most likely where changes in velocity are largest. Though, this variable has no predictive skill (Cliff's delta negligible for both crevassed and highly crevassed areas against crevasse-free areas), which is surprising given that longitudinal extension is the one of the most mentioned mechanisms for crevasse formation (Colgan et al., 2016; Harper et al., 1998; Nye, 1952). Several factors may explain this. Transverse crevasses form under positive longitudinal strain, whereas splaying crevasses form where it is zero or compressive and lateral shear dominates (Harper et al., 1998; Nye, 1952) but we do not distinguish between crevasse types. Strain rate is scale dependent and scales differ across studies. Harper et al. (1998) worked at 20 m, approximately one-fifth of the local ice thickness, Dobler et al. (2023) computed driving stress at 80 m, and our velocity product resolves 50 m. Colgan et al. (2016) identify this scale dependence as a persistent obstacle to comparing field studies. It is moreover unclear that a critical extending strain rate exists. Hambrey and Müller (1978) found crevasses forming below 0.01 $a^{-1}$ and absent above 0.163 $a^{-1}$ and concluded that no such threshold governs new crevasse development, and Colgan et al. (2016) note that inferred critical strain rates vary over three orders of magnitude while critical stresses vary by only a factor of four. Finally, the velocity product carries its greatest uncertainty in the upper accumulation zone, where low surface contrast limits the reliability of feature tracking and determination of flow direction (Rabatel et al., 2023).

Our driving-stress results support the conclusion that stress is the more robust criterion, with highly crevassed areas at a median 70.2 kPa against 49.6 kPa for crevasse-free areas (Cliff's delta 0.22). The spatial gradient in driving stress, which Dobler et al. (2023) proposed as the more physically motivated predictor, did not outperform absolute driving stress in our data (Cliff's delta 0.24 for highly crevassed and 0.10 for crevassed areas), being a second derivative of two independently uncertain fields, it likely accumulates noise faster than information at regional data quality.

https://doi.org/10.5194/egusphere-2026-4768
Preprint. Discussion started: 4 September 2026


Snow-covered areas, which potentially mask crevasses beneath snow bridges, occur where expected at higher elevations, consistent with the seasonal snowline persisting at altitude until the end of the ablation season, and predominantly on flat to concave, low-slope surfaces that favour accumulation over ablation and wind scour. Their higher velocities and along-flow velocity change relative to crevasse-free areas are only superficially unexpected, since the highest velocities occur in the 3000–3250 m band (see Figure A 3 in the appendix) and the median elevation of snow-covered areas (3131 m) falls within it. Driving stress there remains comparable to crevasse-free areas, reinforcing that velocity alone is not a reliable predictor; the combination of low slope, flat-to-concave curvature and low driving stress suggests that most snow-covered terrain is genuinely crevasse-free or only sparsely crevassed. The important implication is that our reference inventory is censored, and censored non-randomly toward high-elevation, low-slope, concave terrain, so the geometric contrasts we report are partly conditioned on detectability. Dobler et al. (2023) note the same limitation, observing that apparent false positives may not be errors where subsurface crevasses are absent from optical reference data.

Finally, three further processes are missing from any predictor built on surface fields calculated within this study. The first is advection. Colgan et al. (2016) describe high-advection lifecycles, in which crevasses form up-glacier and are transported into stress regimes that would not have created them. Our elevated crevasse density on flattening slopes is regional-scale evidence for the former, and accounts for the dense crevassing on the long, low-gradient ablation tongues of the larger valley glaciers, where flat zones of dense crevassing precede steeper slopes (e.g. Ötztal, High Tauern). We hypothesize that reduced healing reinforces this, as sustained melt thins the ice and lowers the overburden pressure that would otherwise close relict crevasses. Though, we are not aware of a published proof of this mechanism. The second is initiation depth. Second, evidence suggests that the fractures which grow into crevasses may start at depths of roughly 15–30 m and spread upward, rather than starting at the surface (Nath and Vaughan, 2003; Colgan et al., 2016). If so, surface geometry only indirectly reflects the conditions that drive fracture, so surface data alone should have limited predictive power regardless of data quality. Third, crevasse formation is also shaped by bed topography, through its effect on basal drag and the resulting stress field, whereas our analysis considers only surface topography; the deeper driver of the patterns we map is therefore not directly observed.

In summary, our results confirm the basic expectation that crevasse density is highest where convex curvature, steep slopes, high driving stress and fast flow occur together, and extend this from individual glaciers to the Austrian glacier population. They also show that these controls act differently. Slope, convex curvature and along-flow slope change increase roughly in step with crevasse density, whereas ice-flow velocity and driving stress act as thresholds that must be crossed before highly crevassed conditions appear. At the same time, our results raise a further question, why along-flow velocity change (representing longitudinal extension) shows no link to crevasse occurrence. Resolving the full strain-rate tensor (shear, longitudinal and transverse strain) rather than the longitudinal component alone will likely be needed to not only account for transverse crevasses but also marginal and longitudinal crevasse fields. Likewise, the temporal behaviour and advection of crevasses cannot be assessed from the single-epoch inventory presented here. A multi-temporal analysis would be needed to disentangle crevasse initiation zones from relict crevasses carried downglacier by advection.

https://doi.org/10.5194/egusphere-2026-4768
Preprint. Discussion started: 4 September 2026


### 4.3 Implications, limitations and future directions

Several limitations on our study exist which should be taken into account when interpreting the results and define clear directions for future work. The most fundamental is the detection of crevasses from optical remote sensing imagery. The mapping relied on optical high-resolution airborne imagery acquired near peak ablation. Hence, only crevasses expressed at the surface were captured and crevasses bridged by snow especially at higher elevations are systematically under-represented. The mapping was performed with the HED-Unet architecture (Baumhoer et al., 2025; Heidler et al., 2021), systematically overpredicting crevasses as shown by a lower precision than recall (86.3% versus 73.7%) over debris covered and rock surfaces due to glacier retreat. By excluding hexagons mostly consisting of debris and rock surface we tried to minimize the effect of overprediction. Furthermore, airborne campaigns on country scale are labour intensive and only performed every couple of years (every four in Austria). This results in the crevasse dataset spanning four years and there is a mismatch e.g. between the mapped crevasses, the velocity, and DEM data. Active microwave sensors offer an additional data source as snow-bridged crevasses can be mapped with synthetic aperture radar, standing out against surrounding snow through enhanced scattering from their side-walls and base. For example, TerraSAR-X has been shown to balance snow penetration against horizontal resolution well enough to locate crevasses in Antarctica (Marsh et al., 2021) but it has to be tested if the spatial resolution is sufficient to map Alpine crevasses as well. Further limitations concern our introduced crevasse density metric as proxy for crevasse occurrence. Because density is defined from crevasse-boundary length within each hexagon, a high value reflects the abundance of crevasse edges rather than crevasse width, depth, or count, nor crevasse orientation.

This study is observation-based and it characterises the crevasse distribution by relating an observed crevasse inventory to observed topographic and ice dynamical variables, rather than by modelling ice deformation or fracture. Its conclusions are therefore associative by identifying the conditions under which crevasses are observed, not the proximate mechanical cause. In particular, we use surface velocity magnitude and gradient change in velocity as observable indicators of the strain-rate field that fracture theory identifies as the driver of crevassing but we do not compute the strain-rate tensor itself. The change in velocity is calculated based on the ice flow velocity data which has major gaps in the middle parts of the glaciers (Rabatel et al., 2023). Especially in these areas transverse crevasses created by longitudinal strain are created but often missed by our analysis due to the data availability limitation.

The different datasets are not exactly contemporaneous and represent snapshots rather than time series, hence, the inventory is best interpreted as a map of crevasse presence under recently observed states. Separating active from relict crevassing, and resolving strain rate directly, would require multi-temporal velocity and crevasse mapping and is left to future work. Finally, by characterising surface topography alone, the analysis represents subsurface and basal controls (e.g. subglacial cavities by circular crevasses, tic-tac-toe crevasse patterns indicate bumps in the bed) only insofar as they are mirrored at the surface. Notwithstanding these constraints, the inventory already demonstrates applied value as it has been incorporated into printed Austrian Alpine Club maps and is well suited to mountaineering geoinformation platforms, while its spatial structure offers a basis for improving surface mass balance modelling by representing latent-heat exchange through crevasses (Colgan et al.,

https://doi.org/10.5194/egusphere-2026-4768
Preprint. Discussion started: 4 September 2026


2016), an independent dataset for mapping strain-rate tensor (Harper et al., 1998) and for spatially consistent crevasse map provides an observational constraint for calibrating or validating damage-mechanics representations of fracture in continuum ice-flow models.

## 5 Conclusion

Crevasses are both a key expression of glacier dynamics but also hazard to field researchers and mountaineers. Yet, their distribution has never been mapped consistently across an entire glacierized mountain region. We present the first spatially consistent, country-scale crevasse inventory for mountain glaciers, covering all Austrian glaciers and linking crevasse density to surface topography and ice flow velocity. Crevasse density varies systematically across the six investigated mountain regions, peaking in the steep, fast-flowing glaciers of the High Tauern and Zillertal Alps and reaching its lowest values on the larger, low-gradient glaciers of the Ötztal and Stubai Alps. By linking a national crevasse inventory to surface topography and ice dynamics, we show that crevasse occurrence is favoured by convex surfaces, steep slopes and along-flow changes in slope (in flattening as well as steepening areas). These geometric controls scale monotonically with crevasse density, whereas ice-flow velocity and driving stress behave as thresholds, distinguishing highly crevassed terrain only once exceeded. We find no relationship between along-flow velocity change and crevasse occurrence, despite longitudinal extension being the mechanism classically invoked. Together with the crevassing observed on flattening slopes, this indicates that a substantial part of the regional crevasse signal is inherited rather than locally generated, and points to advection of relict crevasses which potentially sustained by reduced overburden pressure under continued thinning. Beyond establishing these controls, the inventory provides a practical and scientific resource. It already informs safe route planning in published hiking maps, and it offers an observational basis for representing latent heat exchange by crevasses in surface mass-balance models and for calibrating damage-mechanics fracture schemes in ice-flow models. Future studies should include multi-temporal mapping to track crevasse change in thinning glaciers, analyse crevasse advection and categorize active versus relict crevasse zones. Furthermore, future crevasse maps should be complemented by high-resolution SAR data to recover crevasses hidden beneath snow bridges enabling a more complete mapping of crevasses.

https://doi.org/10.5194/egusphere-2026-4768
Preprint. Discussion started: 4 September 2026


## 2 Appendices

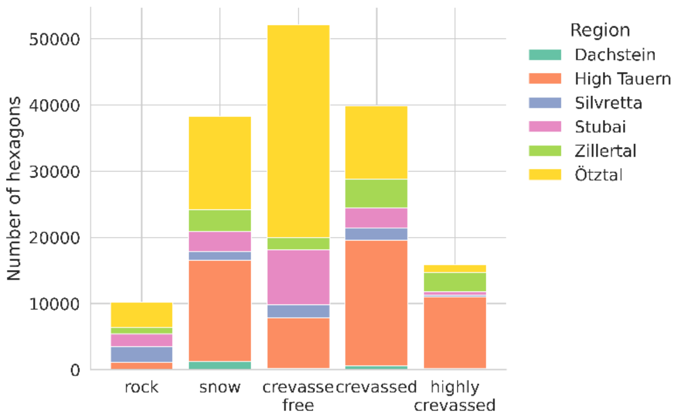


465 **Figure A 1 Bar plot on the number of analysed hexagons per surface class and region.**

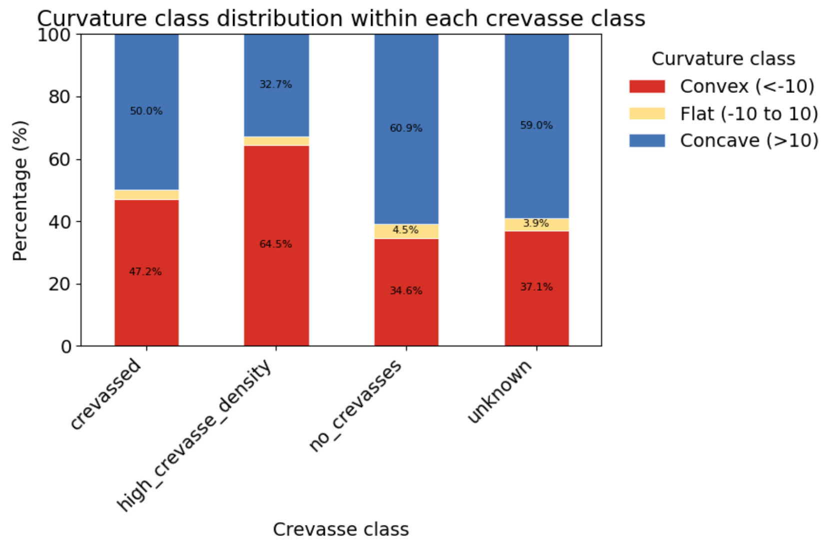


**Figure A 2 Percentage of hexagons within convex, flat and concave slopes for each crevasse class.**

https://doi.org/10.5194/egusphere-2026-4768
Preprint. Discussion started: 4 September 2026


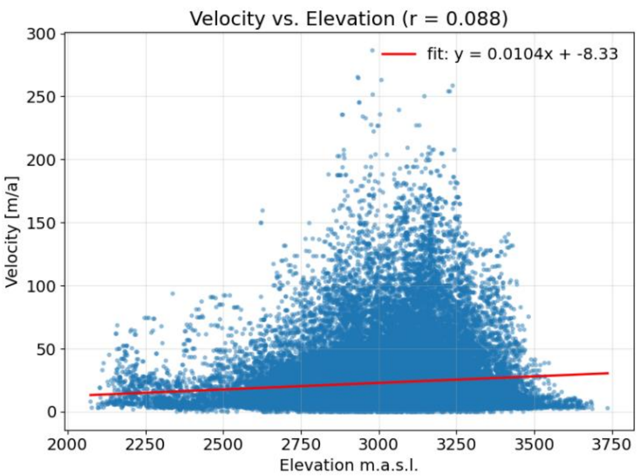


**Figure A 3 Scatterplot of velocity measurements at each elevation based on the analysed hexagons.**

## Code and data availability

The Austrian crevasse dataset is freely available for download at https://doi.org/10.5281/zenodo.20392645 (Baumhoer, 2026). The code for the HED-UNet is provided on GitHub (https://github.com/khdlr/HED-UNet) by Konrad Heidler. Training and validation data used to train the HED-UNet is available at https://doi.org/10.5281/zenodo.20744464 (Baumhoer and Leibrock, 2026). Aerial imagery is freely available by Land Tirol and Land Kärnten which can be downloaded at data.tirol.gv.at and kagis.ktn.gv.at. Glacier boundaries are available from the digital landscape model of Austrian land cover accessible at https://doi.org/10.48677/5db3e58e-3c6b-4bae-98e2-e57e706918da. Basemap.at offers an online GIS of orthophotos over Austria. The GMBA Mountain Inventory v2 is available at https://doi.org/10.48601/earthenv-t9k2-1407 (Snethlage et al., 2021). Ice flow velocity and flow direction data is available at https://entrepot.recherche.data.gouv.fr/dataverse/glacier-velocity (Rabatel et al., 2023). Ice thickness to calculate driving stress was used from Frank et al. (2026).

## Author contributions

C.B. conceived the study, developed the methodology, performed the analysis, produced the figures, and wrote the manuscript. C.B, S.S and S.L. wrote the software. C.M. provided scientific advice and contributed to the interpretation of results. All authors reviewed and edited the manuscript.

## Competing interests

The authors declare to have no competing interests.

## Disclaimer

Copernicus Publications remains neutral with regard to jurisdictional claims made in the text, published maps, institutional affiliations, or any other geographical representation in this paper. While Copernicus Publications makes every effort to include appropriate place names, the final responsibility lies with the authors. Views expressed in the text are those of the authors and do not necessarily reflect the views of the publisher.

## Acknowledgements

We are grateful to basemap.at for providing ortho imagery over Austria. We thank Prof. Dr. Michael Zemp for suggesting the inclusion of an additional "snow" class to account for crevasses hidden by snow bridges and Dr. Konrad Heidler for making the HED-UNet architecture available on GitHub.

## Use of AI

The authors used GitHub Copilot, running GPT-4.1 and Claude Haiku 4.5, to support the development of code for the geospatial analysis and plotting. Language and grammar were improved using Claude (Sonnet 4.6, Opus 4.8) and DeepL Write. All AI-assisted content was reviewed and edited by the authors, who take full responsibility for the final manuscript.

## Financial support

This study was funded by the EO4Alpine Risks project from the German Aerospace Center (DLR).

## References

Barnes, R., 2016. RichDEM: Terrain Analysis Software.
Baumhoer, C., 2026. Inventory of Crevasse Locations on Austrian Glaciers. https://doi.org/10.5281/ZENODO.20392644
Baumhoer, C., Leibrock, S., 2026. Machine Learning Ready Dataset for Glacier Crevasse Detection in Mountain Regions. https://doi.org/10.5281/ZENODO.20744464
Baumhoer, C.A., Leibrock, S., Zapf, C., Beer, W., Kuenzer, C., 2025. Automated crevasse mapping for Alpine glaciers: A multitask deep neural network approach. Int. J. Appl. Earth Obs. Geoinformation 139, 104495. https://doi.org/10.1016/j.jag.2025.104495
BEV, 2024. Digitales Landschaftsmodell - Bodenbedeckung Stichtag 07.05.2024 [dataset]. Bundesamt für Eich- und Vermessungswesen. https://doi.org/10.48677/5db3e58e-3c6b-4bae-98e2-e57e706918da
Bhardwaj, A., Sam, L., Singh, S., Kumar, R., 2016. Automated detection and temporal monitoring of crevasses using remote sensing and their implications for glacier dynamics. Ann. Glaciol. 57, 81–91. https://doi.org/10.3189/2016AoG71A496

https://doi.org/10.5194/egusphere-2026-4768
Preprint. Discussion started: 4 September 2026


Chudley, T.R., Christoffersen, P., Doyle, S.H., Dowling, T.P.F., Law, R., Schoonman, C.M., Bougamont, M., Hubbard, B., 2021. Controls on Water Storage and Drainage in Crevasses on the Greenland Ice Sheet. J. Geophys. Res. Earth Surf. 126, e2021JF006287. https://doi.org/10.1029/2021JF006287

Colgan, W., Rajaram, H., Abdalati, W., McCutchan, C., Mottram, R., Moussavi, M.S., Grigsby, S., 2016. Glacier crevasses: Observations, models, and mass balance implications. Rev. Geophys. 54, 119–161. https://doi.org/10.1002/2015RG000504

Dobler, T., Hagg, W., Mayer, C., 2023. Detection of crevassed areas with minimum geometric information: Vernagtferner case study. J. Glaciol. 69, 1214–1224. https://doi.org/10.1017/jog.2023.12

Eder, K., Reidler, C., Mayer, C., Leopold, M., 2008. Crevasse detection in Alpine areas using ground penetrating radar as a component for a mountain guide system. Int. Arch. Photogramm. Remote Sens. Spat. Inf. Sci. 37, 837–841.

Frank, T., van Pelt, W.J.J., Rounce, D.R., Jouvet, G., Hock, R., 2026. Global glacier-free topography reveals a large potential for future lakes in presently ice-covered terrain. Nat. Commun. 17, 3985. https://doi.org/10.1038/s41467-026-72548-9

Hambrey, M.J., Müller, F., 1978. Structures and Ice Deformation in the White Glacier, Axel Heiberg Island, Northwest Territories, Canada. J. Glaciol. 20, 41–66. https://doi.org/10.3189/S0022143000021213

Harper, J.T., Humphrey, N., Pfeffer, W.T., 1998. Crevasse patterns and the strain-rate tensor: a high-resolution comparison.

Heidler, K., Mou, L., Baumhoer, C., Dietz, A., Zhu, X.X., 2021. HED-UNet: Combined Segmentation and Edge Detection for Monitoring the Antarctic Coastline. IEEE Trans. Geosci. Remote Sens. 60, 1–14. https://doi.org/10.1109/TGRS.2021.3064606

Hösli, L., Ogier, C., Bauder, A., Huss, M., Werder, M.A., Jacquemart, M., Hodel, E., Swift, D.A., Cremona, A., Walden, J., Farinotti, D., 2025. Subglacial cavity collapses on Swiss glaciers: Spatiotemporal distribution and mass loss contribution. J. Glaciol. 71, e74. https://doi.org/10.1017/jog.2025.33

Izeboud, M., Lhermitte, S., 2023. Damage detection on antarctic ice shelves using the normalised radon transform. Remote Sens. Environ. 284, 113359. https://doi.org/10.1016/j.rse.2022.113359

Kirillov, A., Mintun, E., Ravi, N., Mao, H., Rolland, C., Gustafson, L., Xiao, T., Whitehead, S., Berg, A.C., Lo, W.-Y., Dollár, P., Girshick, R., 2023. Segment Anything.

Klocker, E., Meuli, L., Rauch, S., Kottmann, A., Mosimann, U., Pasquier, M., Métrailler, P., Doppman, P., Albrecht, R., Pietsch, U., 2022. Crevasse accidents in the Swiss Alps Epidemiology and mortality of 405 victims of crevasse accidents from 2010 to 2020. Injury 53, 183–189. https://doi.org/10.1016/j.injury.2021.08.010

Lai, C.-Y., Kingslake, J., Wearing, M.G., Chen, P.-H.C., Gentine, P., Li, H., Spergel, J.J., van Wessem, J.M., 2020. Vulnerability of Antarctica's ice shelves to meltwater-driven fracture. Nature 584, 574–578. https://doi.org/10.1038/s41586-020-2627-8

Libert, L., Wuite, J., Nagler, T., 2022. Automatic delineation of cracks with Sentinel-1 interferometry for monitoring ice shelf damage and calving. The Cryosphere 16, 1523–1542. https://doi.org/10.5194/tc-16-1523-2022

Marsh, O.J., Price, D., Courville, Z.R., Floricioiu, D., 2021. Crevasse and rift detection in Antarctica from TerraSAR-X satellite imagery. Cold Reg. Sci. Technol. 187, 103284. https://doi.org/10.1016/j.coldregions.2021.103284

Meissel, K., Yao, E., 2024. Using Cliff's Delta as a Non-Parametric Effect Size Measure: An Accessible Web App and R Tutorial. Pract. Assess. Research, Evaluation Volume 29 Issue 1 2024. https://doi.org/10.7275/PARE.1977

Nye, J.F., 1952. The Mechanics of Glacier Flow. J. Glaciol. 2, 82–93. https://doi.org/10.3189/S0022143000033967

Rabatel, A., Ducasse, E., Millan, R., Mouginot, J., 2023. Satellite-Derived Annual Glacier Surface Flow Velocity Products for the European Alps, 2015–2021. Data 8, 66. https://doi.org/10.3390/data8040066

Ravanel, L., Lacroix, E., Le Meur, E., Batoux, P., Malet, E., 2022. Multiparameter monitoring of crevasses on an Alpine glacier to understand formation and evolution of snow bridges. Cold Reg. Sci. Technol. 203, 103643. https://doi.org/10.1016/j.coldregions.2022.103643

Shankar, S., Stearns, L.A., Veen, C.J. van der, 2023. Semantic segmentation of glaciological features across multiple remote sensing platforms with the Segment Anything Model (SAM). J. Glaciol. 1–10. https://doi.org/10.1017/jog.2023.95

Snethlage, M.A., Geschke, J., Ranipeta, A., Jetz, W., Yoccoz, N.G., Körner, C., Spehn, E.M., Fischer, M., Urbach, D., 2022. A hierarchical inventory of the world's mountains for global comparative mountain science. Sci. Data 9, 149. https://doi.org/10.1038/s41597-022-01256-y

https://doi.org/10.5194/egusphere-2026-4768
Preprint. Discussion started: 4 September 2026


Snethlage, M.A., Geschke, J., Spehn, E.M., Ranipeta, A., Yocco, N.G., Körner, C., Jetz, W., Fischer, M., Urbach, D., 2021. GMBA Mountain Inventory v2: A hierarchical inventory of the world's mountains for global comparative mountain science. https://doi.org/10.48601/EARTHENV-T9K2-1407

Surawy-Stepney, T., Hogg, A.E., Cornford, S.L., Hogg, D.C., 2023. Mapping Antarctic crevasses and their evolution with deep learning applied to satellite radar imagery. The Cryosphere 17, 4421–4445. https://doi.org/10.5194/tc-17-4421-2023

van der Veen, C.J., 1998. Fracture mechanics approach to penetration of surface crevasses on glaciers. Cold Reg. Sci. Technol. 27, 31–47. https://doi.org/10.1016/S0165-232X(97)00022-0

Van Wyk de Vries, M., Lea, J.M., Ashmore, D.W., 2023. Crevasse density, orientation and temporal variability at Narsap Sermia, Greenland. J. Glaciol. 69, 1125–1137. https://doi.org/10.1017/jog.2023.3

Vaughan, D.G., 1993. Relating the occurrence of crevasses to surface strain rates. J. Glaciol. 39, 255–266. https://doi.org/10.3189/S0022143000015926

Xu, T., Yang, W., Liu, Y., Zhou, C., Wang, Z., 2011. Crevasse Detection in Antarctica Using ASTER Images, in: Kamel, M., Campilho, A. (Eds.), Image Analysis and Recognition, Lecture Notes in Computer Science. Springer Berlin Heidelberg, Berlin, Heidelberg, pp. 370–379. https://doi.org/10.1007/978-3-642-21596-4_37

Zamora, R., Casassa, G., Rivera, A., Ordenes, F., Neira, G., Araya, L., Mella, R., Bunster, C., 2007. Crevasse detection in glaciers of southern Chile and Antarctica by means of ground penetrating radar. IAHS Publ.-Ser. Proc. Rep. 318, 152–162.

Zevenbergen, L.W., Thorne, C.R., 1987. Quantitative analysis of land surface topography. Earth Surf. Process. Landf. 12, 47–56. https://doi.org/10.1002/esp.3290120107

Zhao, J., Liang, S., Li, X., Duan, Y., Liang, L., 2022. Detection of Surface Crevasses over Antarctic Ice Shelves Using SAR Imagery and Deep Learning Method. Remote Sens. 14, 487. https://doi.org/10.3390/rs14030487